

## Chapter 6

# Theoretical calculation of $n$ – and $l$ –specific partial cross sections

The fact that direct photoionization and the autoionization of the highly correlated doubly-excited states can interfere renders these process a challenge for theory. This is particularly valid for the evaluation of  $l$ -specific partial cross sections (PCS),  $\sigma_{nl}$ , and angular distribution parameters (ADP),  $\beta_{nl}$ , which are much more sensitive to small deficiencies in the used wave functions than the total cross section (TCS). In addition, some Rydberg series that are weak in the TCS and  $n$ -specific PCSs can be much more intense in the  $l$ -specific PCSs and ADPs; this fact can be very helpful in resolving resonance patterns such as the mirroring behavior discussed in Sect. 5.3.3. These facts have caused substantial interest in  $l$ -specific PCSs and ADPs both from a theoretical and an experimental point of view. Very recently, Harries *et al.* reported on the first analysis of  $l$ -specific PCSs below the  $N = 4$  ionization threshold using a lifetime-resolved fluorescence technique [39, 40]. These measurements of  $l$ -specific PCSs allow a critical test of the theoretical approach, the results of which can be employed to further discuss the mirroring behavior and the mimicking behavior. In addition, reliable  $l$ -specific ADPs are expected to represent a guidance for future experiments, in regions where measurements still are not available.

In section 5.3.3, the mirroring behavior in the PCSs first developed by Liu and Starace [36] was already discussed. We did not find a general mirroring behavior in the PCSs of doubly excited helium, and extended the analytical expression given by Liu and Starace to a more general case in order to understand this finding. We realize that  $\rho^2 \rightarrow 0$  is not a sufficient condition for mirroring behavior. It is additionally necessary that the variations in the PCS are considerably larger than those in the TCS. In the principal series of helium, the variations of the PCSs and those of the TCS are of comparable magnitude, i.e. the observation of a mirroring behavior in some special cases is only accidental, e.g. if one PCS mimics the TCS (see Sect. 5.3). In the following theoretical work, we shall examine the second and third Rydberg series, which that possess  $\rho^2$ -values that are much smaller than these of the principal series. In this way, we are able to further confirm our predictions given in Sect. 5.3.3.

In the following we will discuss shortly the mimicking behavior, which is the opposite of the mirroring behavior and can be found for the case of  $\rho^2 \rightarrow 1$ . If  $\rho^2 \rightarrow 1$ ,  $C_1$  and  $C_2$  in Eq. 3.8 are equal to  $q$  and  $q^2$ , respectively [38, 59]. Then, with Eq. (3.8), the two groups of resonances in the PCSs,  $\sigma_P$  and  $\sigma_Q$ , can be written as

$$\frac{\sigma_P}{\sigma_P^0} = \frac{\sigma_Q}{\sigma_Q^0} = \frac{(q + \epsilon)^2}{1 + \epsilon^2}. \quad (6.1)$$

Obviously, the resonances in the two PCSs,  $\sigma_P$  and  $\sigma_Q$ , mimic each other, and according to this the observation was called mimicking behavior by Liu and Starace [38]. Such a mimicking behavior in the  $n$  and  $l$ -specific ADPs of the principal series can be understood on the basis of that of the  $l$ -specific PCSs. Besides this, one can understand on the basis of such mimicking behavior and an analytical expression of the ADPs, why some resonances cause only rather small variations in the  $l$ -specific ADP in some cases, while – on the other hand – they exhibit pronounced variations in the respective  $l$ -specific PCS. A study of mirroring as well as mimicking behavior can improve the understanding of correlation and decay dynamics in two-electron atoms.

In this chapter, we report on R-matrix calculations of the PCSs,  $\sigma_{nl}$ , and ADPs,  $\beta_{nl}$ , below the single ionization threshold  $I_3$  and  $I_4$  for the photoionization process described with Eq. (3.2). The calculations were performed in  $LS$  coupling, although recent experimental and theoretical studies have shown that spin-orbit interaction has an important influence on the photoionization spectrum very close to the SIT  $I_2$  [42]. However, experimental PCSs and ADPs are not available close to threshold, and the present calculations were restricted to the energy region where the LS-coupling scheme is a good approximation.

## 6.1 R-matrix method

The R-matrix method, which is based on the theory developed by Burke *et al.* [108], has become a quite powerful tool to calculate the interaction of electrons and photons with isolated atoms and their ions. R-Matrix theory [108] starts by partitioning the configuration space into two regions by a sphere of radius  $a$  centered on the target nucleus. In the internal region  $r \leq a$ , electron exchange and correlation between the scattered electron and the  $N$ -electron target are taken into account. The  $(N + 1)$ -electron wave function

$$\Psi_E = \sum_k B_{Ek} \Psi_k \quad (6.2)$$

in the internal region is expanded in terms of energy-independent basis  $\Psi_k$ ,

$$\begin{aligned} \Psi_k = & \mathcal{A} \sum_{ij} c_{ijk} \bar{\phi}_i(x_1, \dots, x_N; \hat{r}_{N+1} \sigma_{N+1}) \frac{1}{r_{N+1}} u_{ij}(r_{N+1}) \\ & + \sum_j d_{jk} \chi_j(x_1, \dots, x_{N+1}), \end{aligned} \quad (6.3)$$

where  $\mathcal{A}$  is the antisymmetrization operator which accounts for electron exchange between the target electrons and the free electron. Note that the energy dependence is described by the coefficients  $B_{Ek}$ .  $\bar{\phi}_i$  are channel functions of the target terms that are included in the close-coupling (CC) expansion and are coupled to the angular and spin functions of the scattered electron. The  $\chi_j$  in the second sum, which vanish at the surface of the internal region, are formed from the bound orbitals of the  $(N + 1)$  system and are included to ensure completeness of the total wave function. The  $c_{ijk}$  and  $d_{jk}$  coefficients in Eq. (6.3) are determined by diagonalizing the  $(N + 1)$ -electron Hamiltonian.

The continuum orbitals  $u_{ij}$  in Eq. (6.3) for each angular momentum  $l_i$  are normally obtained by solving the model single-channel scattering problem

$$\left( \frac{d^2}{dr^2} - \frac{l_i(l_i + 1)}{r^2} + V_0(r) + k_{ij}^2 \right) u_{ij}(r) = \sum_n \Lambda_{ijn} P_{nl_i}(r) \quad (6.4)$$

subject to the fixed boundary conditions

$$u_{ij}(0) = 0 \quad (6.5)$$

$$\left( \frac{a}{u_{ij}(a)} \right) \left( \frac{du_{ij}}{dr} \right)_{r=a} = b. \quad (6.6)$$

The Lagrange multipliers  $\Lambda_{ijn}$  ensure that the continuum orbitals are orthogonal to the bound orbitals  $P_{nl_i}(r)$  of the same angular symmetry.  $V_0(r)$  is a zero-order potential chosen to be the static potential of the target.  $k_{ij}^2$  and  $a$  are the eigenvalues and the radius of the sphere defining the internal region, respectively. The constant  $b$  is arbitrary, and normally set to zero.

The orbital functions  $P_{nl}(r)$  are expressed in slater-type analytical form

$$P_{nl}(r) = \sum_{jnl} C_{jnl} r^{P_{jnl}} \exp(-\xi_{jnl} r) \quad (6.7)$$

and they satisfy the orthonormality conditions:

$$\int_0^\infty P_{nl}(r) P_{n'l'}(r) dr = \delta_{nn'}. \quad (6.8)$$

$C_{jnl}$ ,  $\xi_{jnl}$  and  $P_{jnl}$  are the Clementi-Roetti parameters [109]. In the external region, the colliding electron is outside the atom and a set of coupled differential equations, satisfied by the reduced radial wave functions, are solved subject to the boundary conditions as  $r \rightarrow \infty$ . The two regions are linked by the R-matrix on the boundary ( $r = a$ ) [108].

The R-Matrix method uses the same target orbitals to deal with the initial and final  $(N + 1)$ -electron in the photoionization calculations. The choice of these orbitals for the  $(N + 1)$ -electron system in the first sum of Eq. (6.3) as well as a configuration-interaction expansion for each target state is very crucial. In this dissertation, the CC expansion of the  $\text{He}^+$  target is represented by 20 states obtained from the configurations  $nl$ ,  $n = 1, 2, 3, 4, 5$  and  $l = s, p, d, f, g$  as well as  $\bar{6}s$ ,  $\bar{6}p$ ,  $\bar{6}d$ ,  $\bar{6}f$ ,  $\bar{6}g$ ,  $\bar{6}h$ . The  $1s - 5g$  are exact hydrogen-like wave functions of  $\text{He}^+$  that limit the present calculation below the SIT  $I_4$ . The  $\bar{6}l$  are polarized correlation orbitals of  $\text{He}^+$  and represent electron correlation

Table 6.1: Radial function parameters for  $\text{He}^+$  targets.

orbitals ( $nl$ )	$C_{jnl}$	$P_{jnl}$	$\xi_{jnl}$
$1s - 5g$	hydrogen-like orbitals		
$\bar{6}s$	3.72615	1	0.99478
	-12.31193	2	1.01114
	15.65776	3	0.99832
	-7.40524	4	0.99084
	0.68349	5	0.48055
	-0.37439	6	0.37308
$\bar{6}p$	1.57314	2	2.22668
	-1.28440	3	1.69799
	1.60044	4	0.50277
	-2.42762	5	0.47997
	1.06946	6	0.45202
$\bar{6}d$	1.00608	3	3.69850
	-0.14955	4	1.02029
	0.21028	5	0.42455
	-0.17955	6	0.41004
$\bar{6}f$	0.99998	4	4.78402
	-0.01674	5	0.57790
	0.01191	6	0.44364
$\bar{6}g$	1.00000	5	5.95148
	-0.00036	6	0.43459

optimized on the ground state using the CIVPOL code [110]. The optimized parameters are shown in Table 6.1.

The polarized orbitals included in the target states provide a faster convergence of the wave function in Eq. (6.3) and a better value for the ground state energy. Their effects on photoionization cross sections and resonance properties for the doubly excited states  $^1P^o$  of helium have been discussed in detail in Ref. [111]. In the present case they improve the agreement between the results in length and velocity forms. A crucial choice of the target terms is provided by a calculation of the ground state. The ground state has an energy of  $E = -4 + I_1$  in Rydberg obtained from the variational principle. Table 6.2 lists ionization energies  $I_1$  calculated by the use of different sets of target functions in Refs. [111, 112, 113, 114]. Our calculations lead to an energy of  $-1.80243 \text{ Ry}$  for  $I_1$ , which can be compared with the non-relativistic limit (Pekeris's result) of  $-1.8074 \text{ Ry}$

[112]; the present calculations give obviously better results than other calculations using different target terms.

Table 6.2: Results for the energy of the SIT  $I_1$  of Helium.

States included in expansion	$I_1[\text{Ry}]$	Refs.
1s	-1.7450	Ref. [113]
1s, $\bar{2}p$ , $\bar{3}d$	-1.7817	[113]
1s, 2s, $\bar{2}p$ , 2p, $\bar{3}d$	-1.8007	[113]
1s, 2s, 2p, $\bar{3}p$ , $\bar{3}d$	-1.7868	[114]
1s, 2s, 2p, 3s, 3p, 3d	-1.7732	[111]
1s, 2s, 2p, ..., 4f	-1.7741	[111]
1s, 2s, 2p, ..., 5g	-1.7742	[111]
1s, 2s, 2p, 3s, 3p, 3d, $\bar{4}s$ , $\bar{4}p$ , $\bar{4}d$	-1.7908	[111]
1s, 2s, 2p, ..., 5g, $\bar{6}s$ , ..., $\bar{6}h$ ,	-1.8024	present work
Pekeris's result	-1.8074	[112]

Table 6.3: Results of the present calculations for the effective quantum numbers of the singly excited states  $1sns$  ( $^1S^e$ ) and  $1snp$  ( $^1P^o$ ) of helium. Comparison with experimental results of Moore [115], and the results of calculations based on the R-matrix method by Fernley et al. [114].

$n$	$1sns$ ( $^1S^e$ )			$1snp$ ( $^1P^o$ )		
	theor. results		exp.	theor. results		exp.
	present	Ref. [114]	exp. [115]	present	Ref. [114]	exp. [115]
1	0.74485	0.7481	0.7439			
2	1.85205	1.8579	1.8509	2.01016	2.0101	2.0095
3	2.85799	2.8637	2.8568	3.01203	3.0120	3.0113
4	3.85972	3.8657	3.8585	4.01254	4.0125	4.0118
5	4.86051		4.8593	5.01276		5.0120
6	5.86090		5.8596	6.01287		6.0121
7	6.86115		6.8598	7.01294		7.0121
8	7.86131		7.8602	8.01299		8.0117
9	8.86142		8.8595	9.01302		9.0117
10	9.86149		9.8596			

Tab. 6.3 provides the present effective quantum numbers for the  $1sns$  ( $^1S^e$ ) and  $1snp$  ( $^1P^o$ ) of Rydberg series along with the R-Matrix calculations of Fernley *et al.* [114] and

experimental values of Moore [115], which reveals a good agreement. Further confirmation on the convergence of the CI expansion is provided by the agreement of the length and velocity forms of the present results; this will be discussed in more detail on the basis of the data in the following section. The present configurations and optimized parameters were employed in the calculations of the DCSs below  $I_5$  [116]. In this dissertation, the calculations will be extended to  $n$ - and  $l$ -specific PCSs and ADPs.

## 6.2 Photoionization spectra below $I_3$

The  $l$ -specific PCSs, as compared to the  $n$ -specific PCSs, are much more sensitive to the transition matrix elements, a fact that can be used to further explore the mirroring behavior in  $l$ -specific PCSs. In this section, the mimicking behavior in the ADPs is explained for the first time on the basis of the same behavior in the PCSs.

### 6.2.1 Partial cross sections $\sigma_{nl}$

Below the SIT  $I_3$  of  $\text{He}^+$ , the channels  $n = 1$  and 2 are open resulting in  $\text{He}^+(n = 1)$  and  $\text{He}^+(n = 2)$  final states. In Fig. 6.1, we show the results of the present calculations for the PCSs to these channels and for the total photoionization cross section. The good agreement of the PCSs obtained in the length (solid line) and velocity gauge (dashed line) is due to the high quality of the chosen target wave function. In the discussed energy region, the spectrum includes five resonance series that—in the independent-electron limit—are linear combinations of the configurations  $3sn'p$ ,  $3pn's$ ,  $3pn'd$ ,  $3dn'p$ ,  $3dn'f$ .  $\sigma_1$  consists of  $\cong 90\%$  background cross section due to the strong direct ionization, which decreases strongly with increasing photon energy. The different variations in  $\sigma_1$  and  $\sigma_2$  caused by the principal series  $3, 1_{n'}$  can be regarded as a consequence of different changes of the nodal structure of the wave function in the decay process according to the so-called propensity rules [33, 31], which were discussed in more details in Sect. 5.3.2.

The resonances  $3, -1_3$  and  $3, 2_4$ , which is plotted in magnified form in the inset, are good examples for testing our predictions for mirroring behavior. Although  $\rho^2$  is very small, namely 0.016 for  $3, -1_3$  and 0.001 for  $3, 2_4$ , the two resonances do not show mirroring behavior between  $\sigma_1$  and  $\sigma_2$ , in contrast to the prediction of Liu and Starace [36]. Moreover,  $3, -1_3$  shows mimicking behavior. As described above, the absence of mirroring behavior can be understood on the basis of the analytical expression derived in Sect. 5.3.3 as well as by the fact that the variations in the TCS caused by these two resonances are of the same order of magnitude as those of  $\sigma_1$ . Compared to previous calculations, the present results—shown in Fig. 6.1—are in good agreement with the K-matrix  $L^2$ -basis-set calculations of Moccia and Spizzo [117]. They are in between the results of calculations in the length form and in the velocity form obtained by Salomonson [118], with many-body perturbation theory.

In Fig. 6.2, the theoretical results are convoluted with a Gaussian describing the appropriate photon band pass in order to facilitate a comparison with experimental

spectra. In Fig. 6.2(a), results of two measurements of the TCS, taken with a resolution of 4 meV (FWHM) [30] and 35 meV [34], respectively, are given. For the data of Domke *et al.* [30], taken with higher resolution and better signal-to-noise ratio, the cross section is given only in arbitrary units. Figure 6.2(b) and (c) show the experimental PCSs of Menzel *et al.* [34] measured with a resolution of 35 meV (FWHM). In Fig. 6.2(c), the results of Ref. [103], obtained with a resolution of 170 meV, are also plotted. It can be seen that the result of the present calculations agree well with the experimental data what resonance position, lineshape, and width are concerned. The TCS and the PCS  $\sigma_1$  are about 5% larger than the only existing absolute experimental cross sections reported

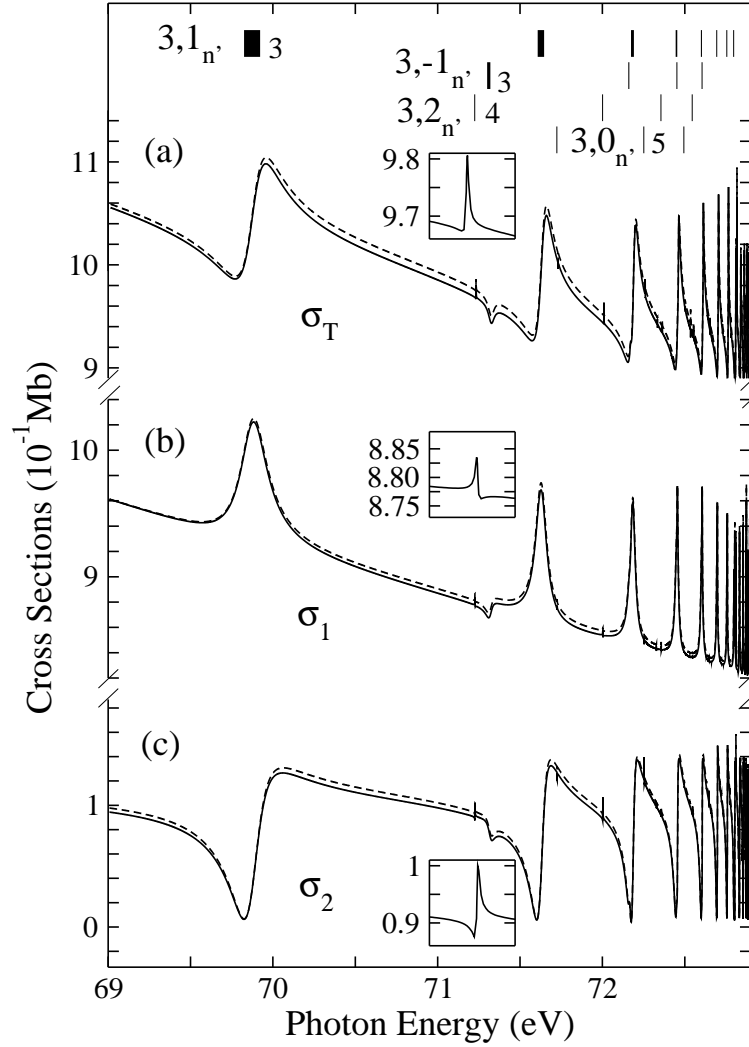


Figure 6.1: (a) Total photoionization cross section  $\sigma_T$  in the photon-energy region from 69.1 to 72.8 eV. In (b) and (c), the partial cross sections  $\sigma_1$  and  $\sigma_2$  are displayed. The solid lines and dashed lines represent the results obtained in the length form and in the velocity form, respectively. The insets give the resonance  $3,2_4$  in the energy region from 71.22 to 71.25 eV on a magnified scale. The vertical bar diagrams in the upper part of the figure represent the assignment of the double-excitation resonances as obtained from theoretical calculations [31]. The widths of the vertical bars are proportional to the resonant linewidths.

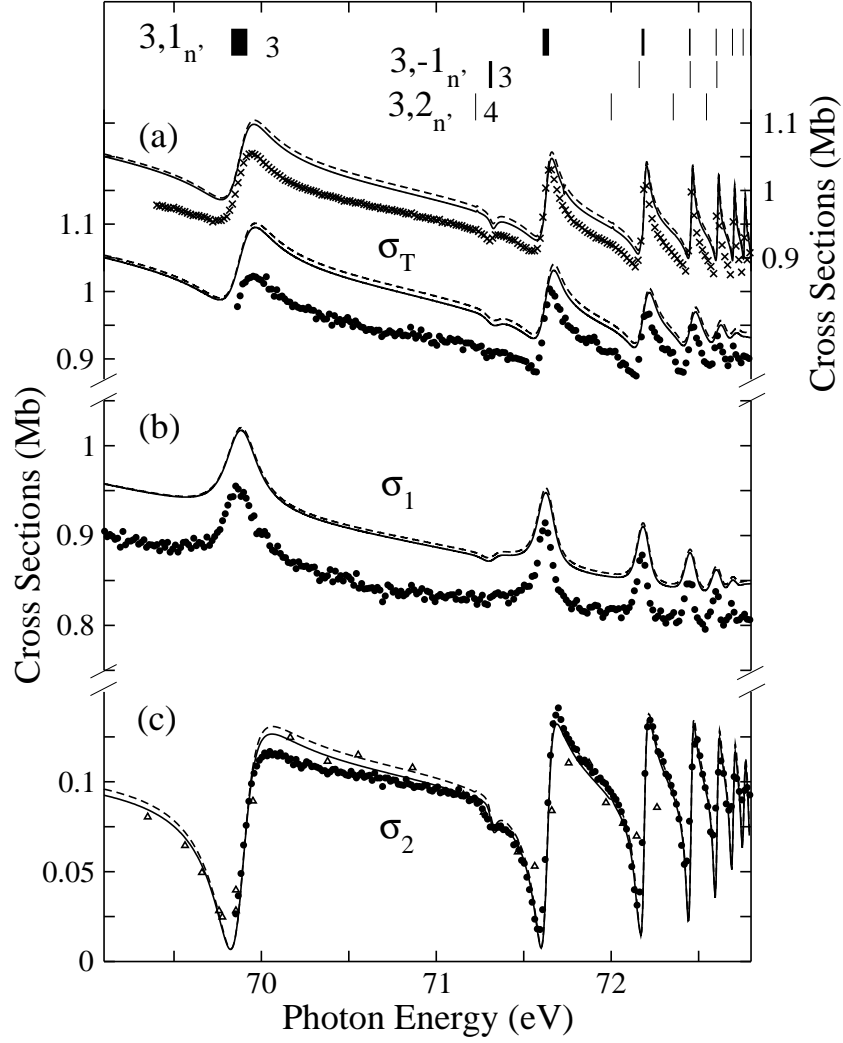


Figure 6.2: (a) Total cross section convoluted with a Gaussian of 4 meV (FWHM) (upper curves related to the right axis) and 35 meV (lower curve, related to left axis) in the energy region from 69.1 to 72.8 eV. (b) and (c) Partial cross sections  $\sigma_1$  and  $\sigma_2$  convoluted with a Gaussian of 35 meV.  $\times$ , relative experimental data from Ref. [30],  $\bullet$ , from Ref. [34],  $\triangle$ , from Ref. [103]; further, for details, see Fig. 6.1.

by Menzel *et al.* [34]. However, excellent agreement is also found between the present calculations and the hyperspherical close-coupling calculations reported by Menzel *et al.* [34]. The resonance  $3,-1_3$  is better resolved in the experimental cross section  $\sigma_2$ , which means that this resonance has a stronger coupling to the ionization channel  $n = 2$ .

Figure 6.3(b) and (c) displays the PCSs leading to the final ionic states  $\text{He}^+(2s)$  and  $\text{He}^+(2p)$ . These calculated PCSs exhibit excellent agreement with recent data of Harries *et al.* [40]. Compared with the cross section  $\sigma_2$  in Fig. 6.3(a), the PCSs  $\sigma_{2s}$  and  $\sigma_{2p}$  exhibit clearer and richer resonance structures. The clearer resonance structures in the PCSs  $\sigma_{2s}$  and  $\sigma_{2p}$  of the various secondary series are accompanied by a mirroring behavior for these resonances. This can be understood by the fact that the sum of any two PCSs can be expressed by the Fano formula. Note that in this case  $\rho^2$  can still be regarded



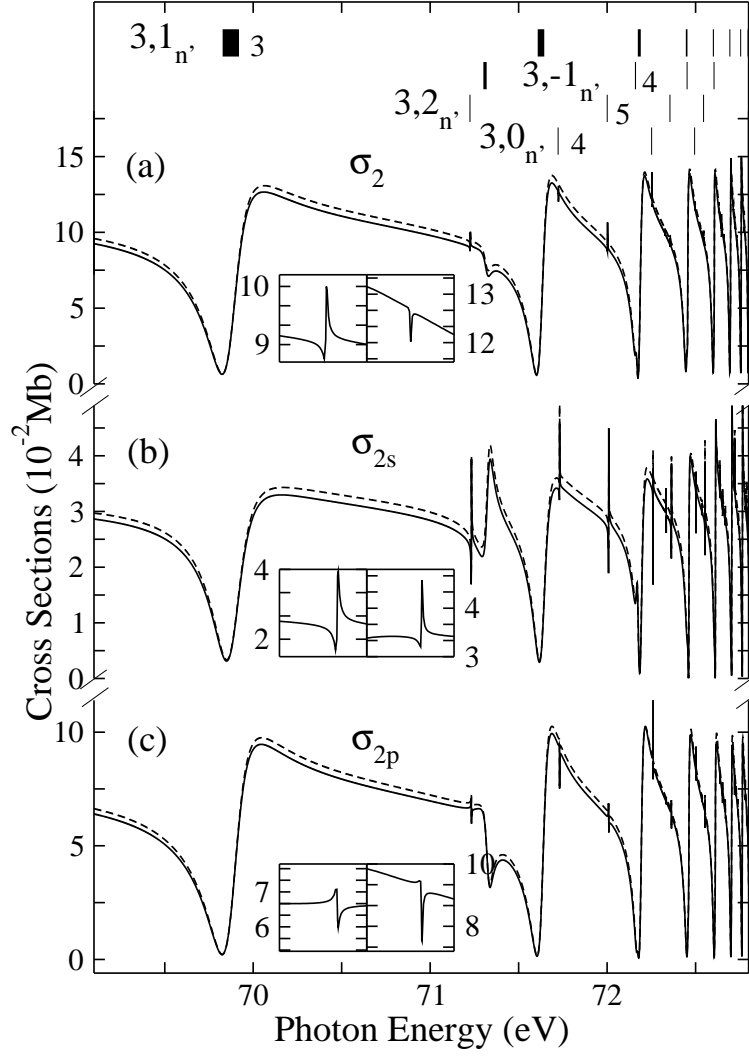


Figure 6.3: Partial photoionization cross sections (a)  $\sigma_2$ , (b)  $\sigma_{2s}$ , and (c)  $\sigma_{2p}$  in the energy region from 69.1 to 72.8 eV. The left insets show the resonance  $3,2_4$  in the energy region from 71.20 to 71.25 eV in magnified form, while the right insets show the  $3,0_4$  resonance in the energy region from 71.70 to 71.75 eV. For further details, see Figs. 6.1 and 6.2.

as the maximum fractional depth of the minimum in the vicinity of a resonance in the sum of two individual PCSs. It loses its physical meaning defined by the Fano profiles for the TCSs, however. As a result, the analysis given in Sect. 5.3 can be employed to discuss and understand the mirroring and mimicking behaviors of any two individual PCSs although the sum of them are not the TCS, such as obtained in case of  $\sigma_{2s}$  and  $\sigma_{2p}$  (see Fig. 6.3). Because of  $\rho^2 \rightarrow 1$ , the resonances of the principal series  $3,1_{n'}$  mimic each other in  $\sigma_{2s}$  and  $\sigma_{2p}$ , as expected by Liu and Starace [36]. Most of the secondary series exhibit  $\rho^2 \rightarrow 0$  and show much stronger variations in  $\sigma_{2s}$  and  $\sigma_{2p}$  than in  $\sigma_2$ , so that the prerequisites for mirroring behavior are fulfilled [37, 36]. The insets in Fig. 6.3 show that the resonances  $3,2_4$  and  $3,0_4$  actually display a mirroring behavior.

### 6.2.2 Angular distribution parameters $\beta_{nl}$

As compared to the PCSs, the ADPs show different dependences on the matrix elements for excitation and decay of the autoionization states. This can lead to the situation that a resonance is clearly seen in the PCSs but not in the ADPs or vice versa. In particular, the ADPs depend also on the phases of the matrix elements. In the LS-coupling scheme, the  $l$ -specific ADPs,  $\beta_{nl}$ , depend on the matrix elements and phase differences between the two different partial waves  $\varepsilon(l-1)$  and  $\varepsilon(l+1)$  of the outgoing electrons. The ADPs can be expressed in an effective spherically symmetric potential by [119]

$$\beta_{nl} = \frac{l(l-1)R_{nl,\varepsilon(l-1)}^2 + (l+1)(l+2)R_{nl,\varepsilon(l+1)}^2}{(2l+1)[lR_{nl,\varepsilon(l-1)}^2 + (l+1)R_{nl,\varepsilon(l+1)}^2]} \quad (6.9)$$

$$- \frac{6l(l+1)R_{nl,\varepsilon(l-1)}R_{nl,\varepsilon(l+1)}\cos(\delta_{l+1} - \delta_{l-1})}{(2l+1)[lR_{nl,\varepsilon(l-1)}^2 + (l+1)R_{nl,\varepsilon(l+1)}^2]}, \quad (6.10)$$

with  $R_{nl,\varepsilon(l\pm 1)}$  being the radial integrals and  $\delta_{l\pm 1}$  the background phases that can be considered to be constant in the region of the resonance [46]. Note that  $\sigma_{nl} \propto lR_{nl,\varepsilon(l-1)}^2 + (l+1)R_{nl,\varepsilon(l+1)}^2$ .

The interaction of a bound state with a continuum leads to an increase in the phase of the continuum wave function. The resulting effects on  $\sigma_{nl}$  and  $\beta_{nl}$  are described by the  $R_{nl,\varepsilon(l\pm 1)}$ , which – in the vicinity of a resonance – depend strongly on energy; the corresponding variations in  $R_{nl,\varepsilon(l\pm 1)}^2$  can be parametrized by the Fano formula. In the following we shall briefly discuss the possibility of different behaviors of  $\sigma_{nl}$  and  $\beta_{nl}$  in the vicinity of a resonance. By assuming perfect mimicking of a resonance in  $\sigma_{nl,\varepsilon l+1}$  and  $\sigma_{nl,\varepsilon l-1}$ , i.e.  $\sigma_{nl,\varepsilon l-1} = c^2 \cdot \sigma_{nl,\varepsilon l+1}$  and  $R_{nl,\varepsilon l-1} = c \cdot R_{nl,\varepsilon l+1}$ , with  $c$  being a constant value, one obtains

$$\begin{aligned} \beta_{nl} &= \frac{[l(l-1) \cdot c^2 + (l+1)(l+2) - c \cdot 6l(l+1)\cos(\delta_{l+1} - \delta_{l-1})]}{(2l+1)(c^2 \cdot l + l + 1)} \\ &= \text{const.} \end{aligned} \quad (6.11)$$

From this we can conclude that resonances with strong variations in  $\sigma_{nl}$  may cause only small variations in  $\beta_{nl}$  if  $\sigma_{nl,\varepsilon l+1}$  mimics  $\sigma_{nl,\varepsilon l-1}$ . A good example for this is the resonance  $4,0_4$  that exhibits a strong variation in  $\sigma_{3d}$  (see Fig. 6.9), but only small variations in  $\beta_{3d}$  (see Fig. 6.11), as discussed above. Unfortunately, the corresponding PCSs  $\sigma_{3d,\varepsilon p}$  and  $\sigma_{3d,\varepsilon f}$  are not available from calculations so that the assumed mimicking behavior cannot be verified. If  $\sigma_{nl,\varepsilon(l+1)}$  and  $\sigma_{nl,\varepsilon(l-1)}$  show a mirroring behavior, the numerator and denominator of equation (6.10) change independently. Under these conditions we found in simulations that  $\beta_{nl}$  can vary strongly in the resonance region although there are no variations in  $\sigma_{nl}$ .

In LS coupling, all ADPs  $\beta_{ns}$  are identical to 2. Therefore, in Fig. 6.4 we only display the results for  $\beta_2$  and  $\beta_{2p}$  below the SIT  $I_3$ . In this figure, the results for  $\beta_2$  and  $\beta_{2p}$  of both calculations (length form and velocity form) are almost identical, revealing again the quality of the target states used in the calculations. All five Rydberg series can

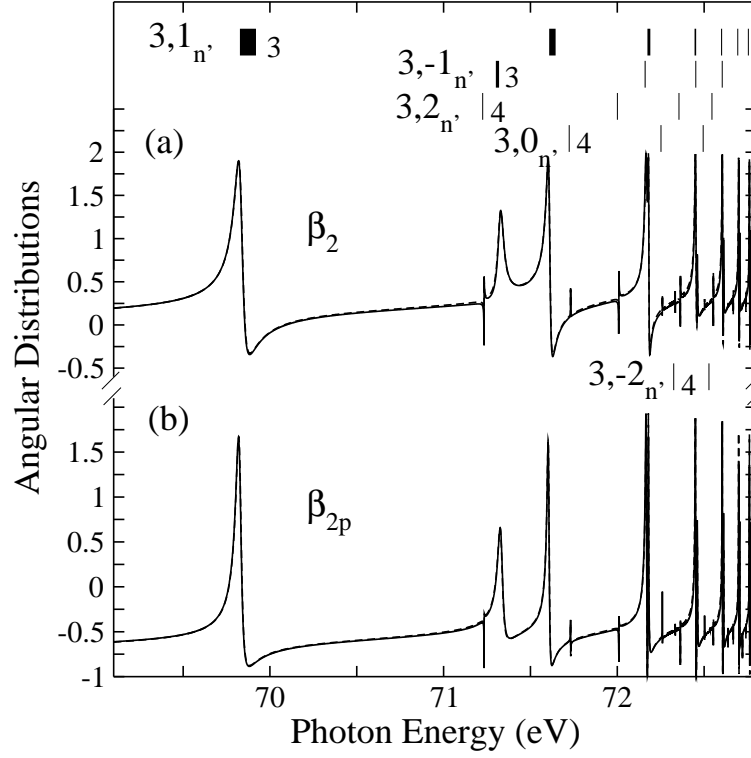


Figure 6.4: Angular distribution parameters (a)  $\beta_2$  and (b)  $\beta_{2p}$  in the energy region from 69.1 to 72.8 eV. For further details, see Fig. 6.1.

be clearly seen in the curves for  $\beta_2$  and  $\beta_{2p}$ . Because of the mimicking behavior of  $\sigma_{2s}$  and  $\sigma_{2p}$  in the series  $3, 1_{n'}$ , i.e.  $\rho^2 \rightarrow 1$ , we readily obtain from Eq. (6.1) the relation  $\beta_2 = (2\sigma_{2s}^0 + \sigma_{2p}^0 \beta_{2p}) / \sigma_2^0$ . Based on this expression, we then realize that  $\beta_2$  and  $\beta_{2p}$  exhibit a similar energy dependence, and the mimicking behavior of  $\beta_2$  and  $\beta_{2p}$  for the principal series  $3, 1_{n'}$  can be readily understood. The mimicking of resonance  $3, -1_3$  in  $\beta_2$  and  $\beta_{2p}$ , however, is expected to be accidental due to the accidental mirroring behavior of  $\sigma_{2s}$  and  $\sigma_{2p}$ . Compared to previous theoretical calculations [117, 118], the present results generally reflect good agreement in magnitudes, peak positions, and line shapes. It should be noted that in the calculations of Sánchez and Martín [120], the principal series  $3, 1_{n'}$  show an almost symmetric variation in the  $\beta_{2p}$ , while we find a rather asymmetric profile for these series.

The present results for the angular distribution parameters, convoluted with a Gaussian of 12 meV width, and the previously published results of the high resolution measurements of  $\beta_2$  by Menzel *et al.* [34] are presented in Fig. 6.5. The experimental results of Zubek *et al.* [122], measured with a resolutions of 60 meV, and those of Lindle *et al.* [103], recorded with a resolution of 170 meV, are also given. In general, a good agreement between theory and experiments can be observed. However, with increasing photon energy, the values of Menzel *et al.* decrease in magnitude as compared to those of Zubek *et al.*. Close to the  $N = 3$  ionization threshold, the ADPs of Menzel *et al.* are by  $\cong 0.2$  lower than those of Zubek *et al.*, with the latter agreeing better with the present theoretical results. It should be noted that recent studies proved the geometry to be

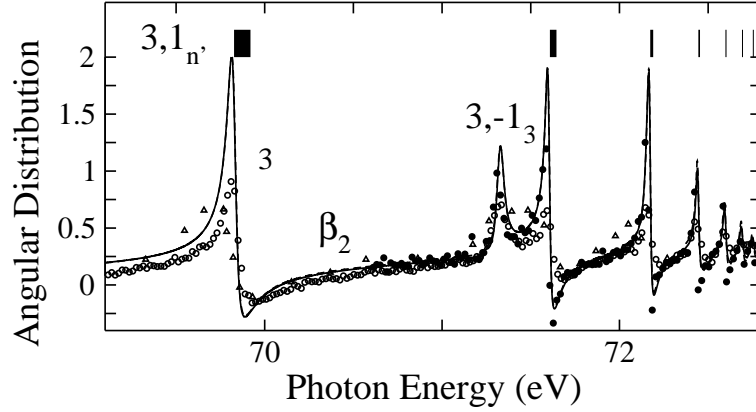


Figure 6.5: Angular distribution parameter  $\beta_2$  in the energy region from 69.1 to 72.8 eV convoluted with a Gaussian of 12 meV. ●, experimental data from Ref. [34], △, from Ref. [103], ○, from Ref. [122]. For further details, see Fig. 6.1.

important for measurements of the  $\beta$ -parameter. In particular, for a  $\beta$  determination, the measurements have to be done in the plane perpendicular to the direction of the photon beam. Contributions from out of this plane, caused by non-dipolar effects, can lead to wrong values of  $\beta$  [123, 124]. These non-dipolar effects in the angular distribution have been utilized by Krässig *et al.* [125] to detect the dipole-forbidden doubly excited resonances  $^1D_2(2p^2)$  of helium. Such contributions of non-dipolar effects cannot be excluded as an explanation for the difference between theory and experimental by Menzel *et al.*, since no information was provided on the detection geometry in Ref. [35]. The present results and all available experimental data confirm clearly the observation of the state  $3,-1_3$  in the spectrum.

## 6.3 Photoionization spectra below $I_4$

### 6.3.1 Partial cross sections $\sigma_{nl}$

The TCS  $\sigma_T$  and PCSs  $\sigma_1$ ,  $\sigma_2$ ,  $\sigma_3$  for the photoionization processes below the SIT  $I_4$  that lead to the channels  $n = 1, 2$ , and  $3$  are presented in Fig. 6.6(a-d). The results obtained in the velocity form are by  $\cong 0.4$  to  $3.8\%$  larger in magnitude than those calculated in the length form; the shapes of the two curves, however, are almost identical. As observed for the states below the ionization threshold  $I_3$ , the channel  $n = 1$  is the most intense one due to strong contributions of direct photoionization dominating the TCS. Analogous to the situation below  $I_3$ , the PCS  $\sigma_1$  decreases quickly with increasing photon energy. All other resonance series besides the principal series are quite weak in the PCSs  $\sigma_n$ .

In Fig. 6.7(a), we show convoluted theoretical TCS and PCSs below  $I_4$ , together with experimental results: the cross section in the upper part is convoluted with a Gaussian of 4.0 meV (FWHM) in order to allow a comparison with the relative experimental cross sections of Domke *et al.* [30]; in the lower part, the theoretical cross section is convoluted with a Gaussian of 35 meV (FWHM) to compare with the absolute cross sections of

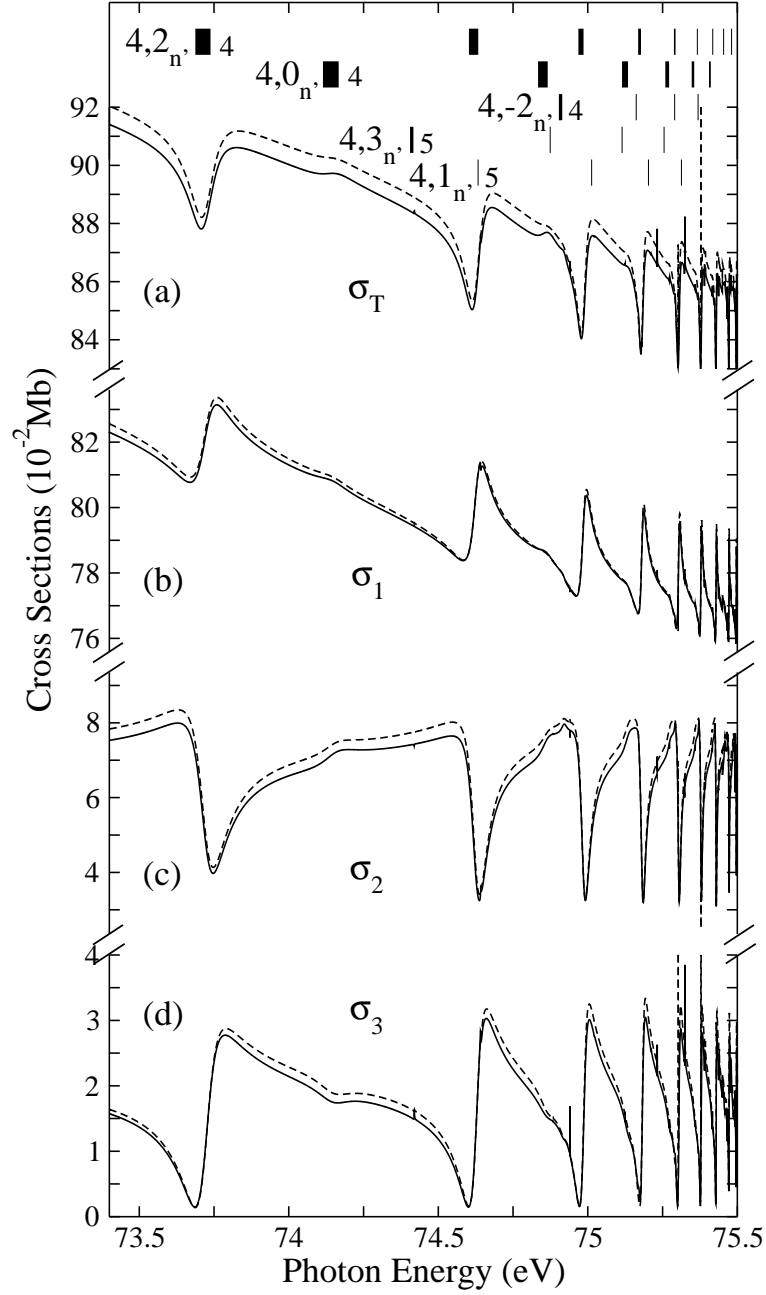


Figure 6.6: (a) Total cross section  $\sigma_T$ , (b) to (d) partial cross sections  $\sigma_1$  to  $\sigma_3$  in the energy region from 73.4 to 75.5 eV. For further details, see Fig. 6.1.

Menzel *et al.* [34]. The theoretical results agree well with the experimental results of Domke *et al.*, that revealed an asymmetric line shape with  $q > 0$  for the principal series  $4,2_{n'}$ . In the experiments of Menzel *et al.*, however, the resonance profiles of the  $4,2_{n'}$  series exhibit a ‘window-like’ lineshape, i.e.  $q \cong 0$ . In a direct comparison, the present theoretical cross sections agree within 6% with the only available absolute experimental results. This deviation slightly exceeds the combined error bars of the experimental and the theoretical data. The accuracy in the measurement of Menzel *et al.* is about 2% for  $\sigma_1$ , 10% for  $\sigma_2$ , and 13% for  $\sigma_3$ . In addition, the present theoretical resonance positions

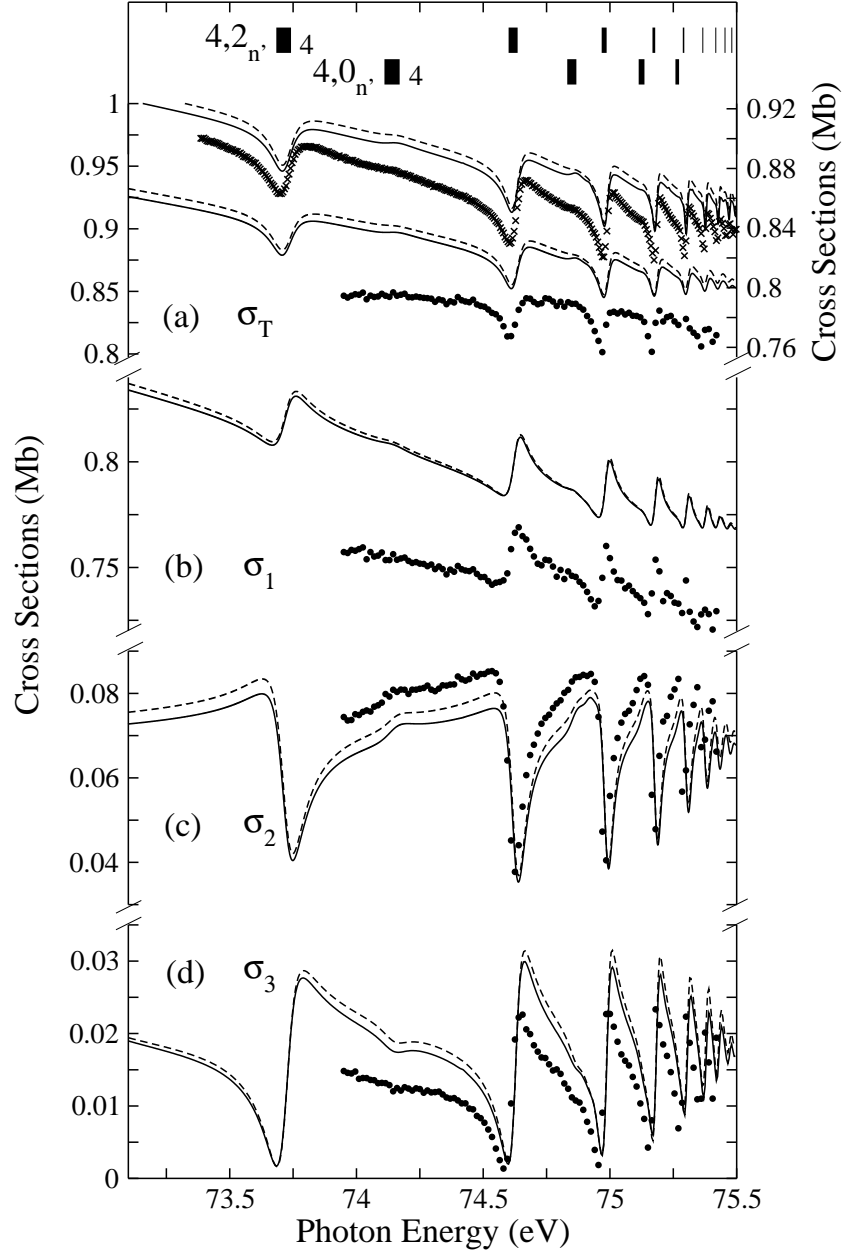


Figure 6.7: (a) TCS convoluted with a Gaussian of 4 meV (FWHM) (upper curves with scale on right ordinate) and 35 meV (lower curves with scale on left ordinate) in the energy region from 73.4 to 75.5 eV. (b) to (d), PCSs  $\sigma_1$ ,  $\sigma_2$ , and  $\sigma_3$  convoluted with a Gaussian of 35 meV.  $\times$ , related experimental data from Ref. [30],  $\bullet$ , from Ref. [34]. For further details, see Figs. 6.1.

are shifted slightly to higher energies by about 40 meV as compared to the experimental data. The present theoretical result as well as the calculations of Ref. [34] agree very well with regard to intensities, line widths, and shapes of the resonances; however, Menzel *et al.* gave no details of their calculations.

The theoretical  $l$ -specific PCSs  $\sigma_{2s}$ ,  $\sigma_{2p}$ ,  $\sigma_{3s}$ ,  $\sigma_{3p}$ , and  $\sigma_{3d}$  are displayed in Figs. 6.8 and 6.9, together with the corresponding  $n$ -specific PCSs  $\sigma_2$  and  $\sigma_3$ . The PCSs  $\sigma_{np}$  dominate the PCSs  $\sigma_2$  and  $\sigma_3$  in Figs. 6.8 and 6.9 because of the strong coupling of the ground

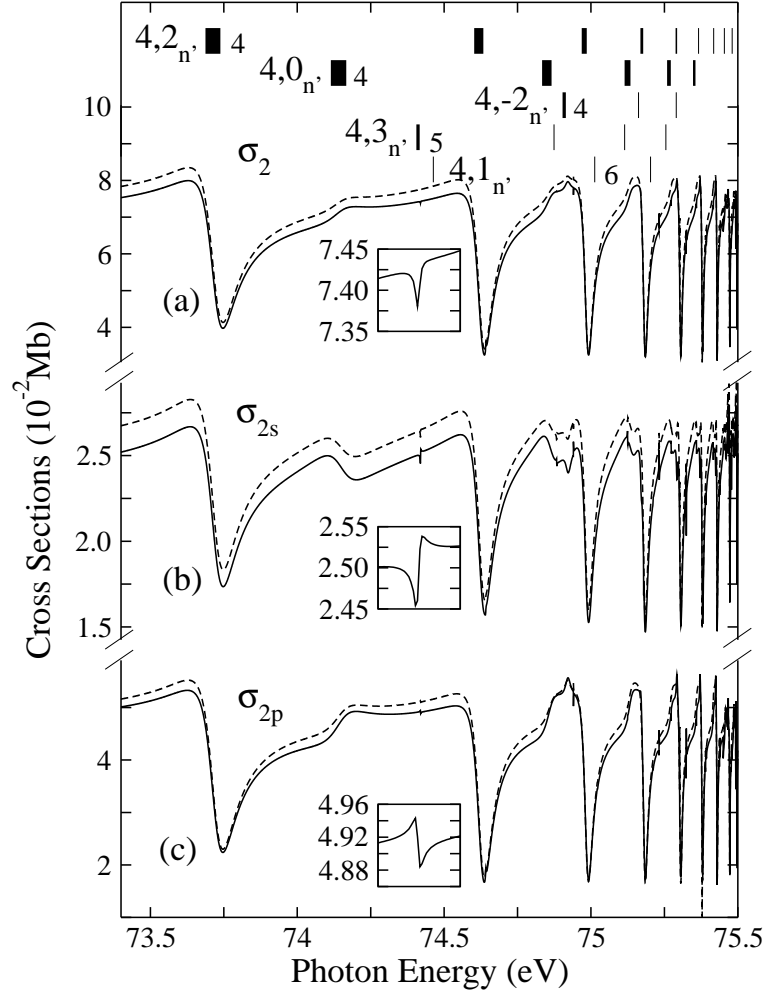


Figure 6.8: Partial photoionization cross sections (a)  $\sigma_2$ , (b)  $\sigma_{2s}$ , and (c)  $\sigma_{2p}$  in the energy region from 73.4 to 75.5 eV. The insets show the resonance  $4, 3_5$  in magnified form in the energy region from 74.41 to 74.43 eV. For further details, see Figs. 6.1 and 6.2.

state and the continuum states  $2pn'l'$  and  $3pn'l'$ . The expected similarities in the  $\sigma_{nl}$  of the principal series have also been shown in Figs. 6.8 and 6.9, which can be explained by mimicking behavior. The overall agreement with the calculations of Sánchez and Martín [120] and with those of Hayes and Scott [121] is reasonable. However, in our calculations,  $\sigma_{3d}$  dominates over  $\sigma_{3s}$  in the entire energy region, while in the calculations of Hayes and Scott, the  $\sigma_{3d}$  partial cross section was consistently smaller than the  $\sigma_{3s}$  cross section at energies above 74.6 eV. Sánchez and Martín reported completely opposite results.

Very recently, Harries *et al.* [39] reported on the first measurements of  $l$ -specific PCSs  $\sigma_{2s}$ ,  $\sigma_{2p}$ ,  $\sigma_{3s}$ ,  $\sigma_{3p}$ , and  $\sigma_{3d}$  below  $I_4$  using a lifetime-resolved fluorescence technique; statistically improved data were later presented in Ref. [40]. The measurements of Ref. [39] are displayed in Fig. 6.10 along with the present calculations convoluted with a Gaussian of 10 meV (FWHM) in order to simulate the experimental resolution of the experiments. The relative intensities of the measurement are given on the right ordinate axis. The excellent agreement between theory and experiment confirms the high quality

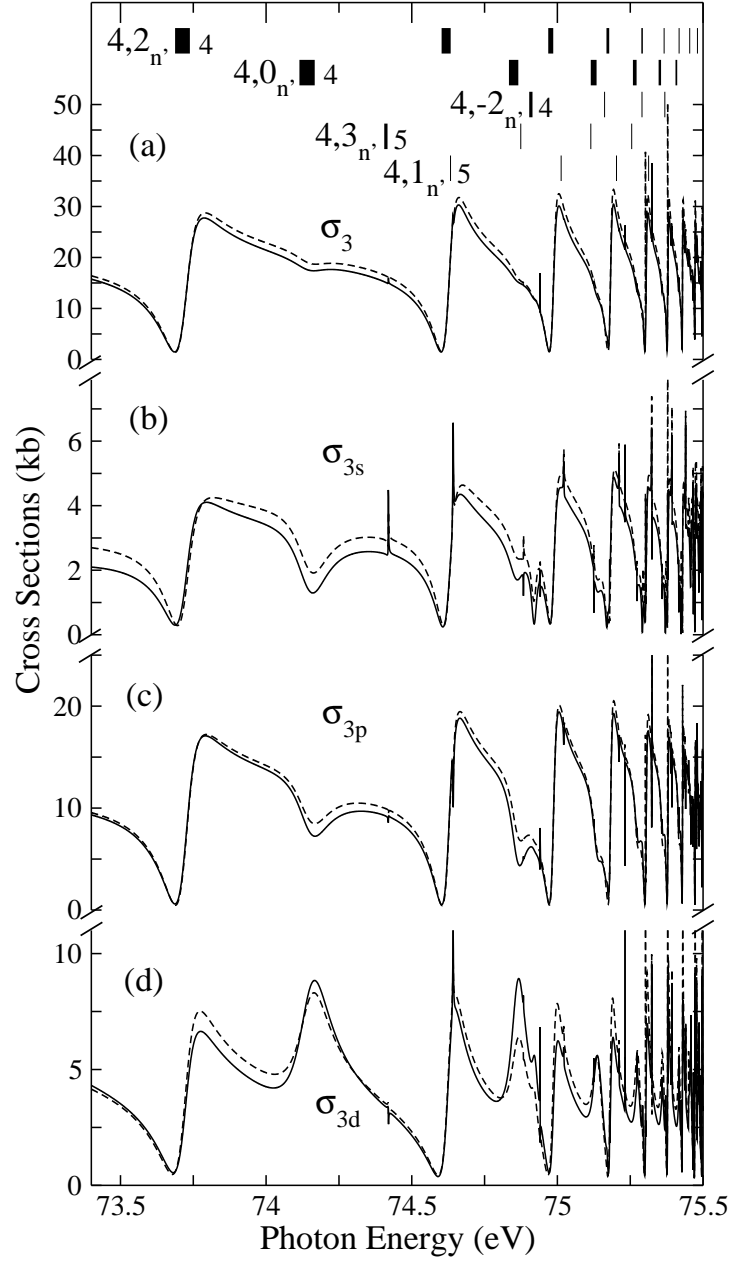


Figure 6.9: Partial photoionization cross sections (a)  $\sigma_3$ , (b)  $\sigma_{3s}$ , (c)  $\sigma_{3p}$ , and (d)  $\sigma_{3d}$  in the energy region from 73.4 to 75.5 eV. For further details, see Figs. 6.1 and 6.2.

of the performed calculations. In the PCS  $\sigma_{3d}$ , the secondary series  $4,0_{n'}$  shows the strongest coupling to this ionization channel. Therefore, the resonances  $4,0_{n'}$  can be observed from  $n' = 4$  to 8, which is shown in Fig. 6.10(e), with good agreement between experiment and theory. The experimental observations of the first resonance of the series  $4,-2_{n'}$  also agree well with the present calculations. The first resonance of the  $4,3_n$  series, namely  $4,3_5$ , is clearly visible in the theoretical partial cross section  $\sigma_{3s}$  convoluted with a Gaussian of 10 meV (FWHM); it also seems to be reproduced in the experimental results, although it is not discussed by the authors. However, the noise in the experiment is comparable to the expected intensity of the resonance  $4,3_5$ , i.e. the



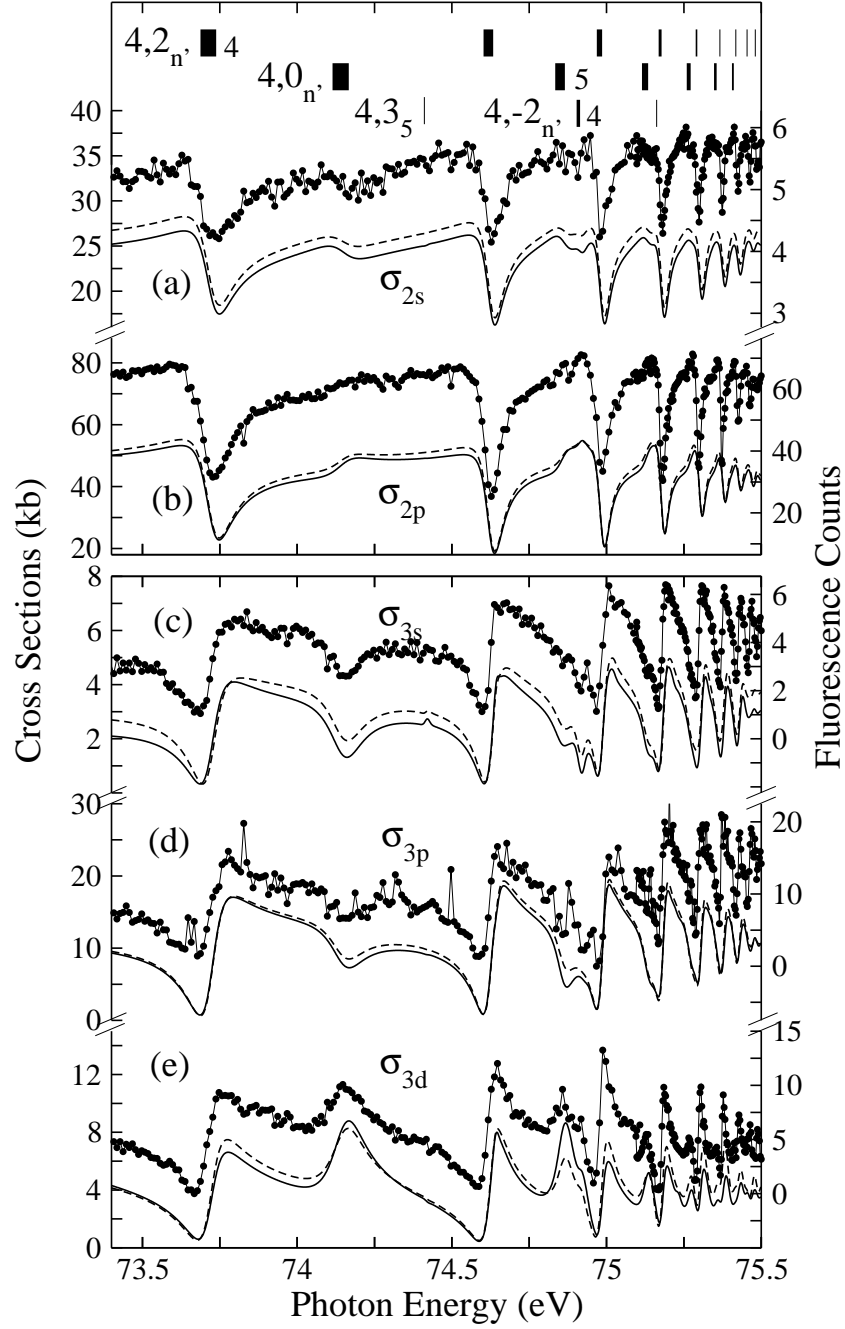


Figure 6.10: (a)  $l$ -specific partial photoionization cross sections  $\sigma_{2s}$ ,  $\sigma_{2p}$ ,  $\sigma_{3s}$ ,  $\sigma_{3p}$ , and  $\sigma_{3d}$  convoluted with a Gaussian of 10 meV (FWHM) in the energy region from 73.4 to 75.5 eV (scale on left ordinate). The data points, connected by straight solid line (scale on right ordinate), represent experimental data from Ref. [39]. For further details, see Figs. 6.1 and 6.2.

observation of this resonance is not unambiguous. More recent experimental results [40], with improved signal-to-noise ratio, however, confirm the existence of the resonance  $4, 3_5$ . These recent data also show in general a better agreement with the present theoretical results. This is in particular valid for the resonance  $4, 0_5$  in  $\sigma_{3p}$ . The lineshapes of the present calculations agree better with these measurements than those of Sánchez and

Martín shown in Ref. [39], in particular in case of  $\sigma_{3d}$ . The relative magnitudes from the measurements demonstrate that the PCS  $\sigma_{3d}$  always dominates over  $\sigma_{3s}$ , an observation that agrees well with our results, as discussed above.

### 6.3.2 Angular distribution parameters $\beta_{nl}$

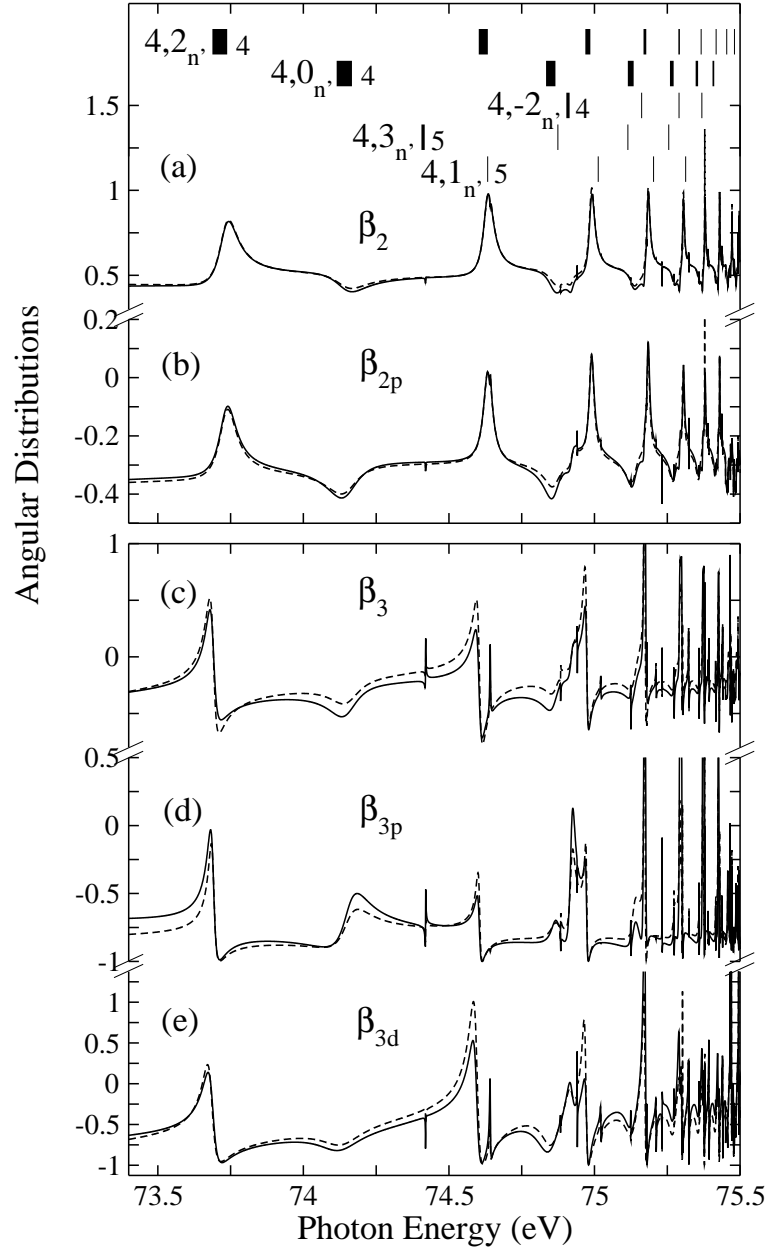


Figure 6.11: Angular distribution parameters (a)  $\beta_2$ , (b)  $\beta_{2p}$ , (c)  $\beta_3$ , (d)  $\beta_{3p}$ , and (e)  $\beta_{3d}$  in the energy region from 73.4 to 75.5 eV. For further details, see Fig. 6.1.

The theoretical ADPs  $\beta_2$ ,  $\beta_{2p}$ ,  $\beta_3$ ,  $\beta_{3p}$ , and  $\beta_{3d}$  below  $I_4$  are presented in Fig. 6.11(a-e). The 7 overlapping resonance series cause all comparable variations in  $\beta$  and this makes it very difficult to discuss the resonances separately, in particular in the  $l$ -specific  $\beta_{3l}$ .

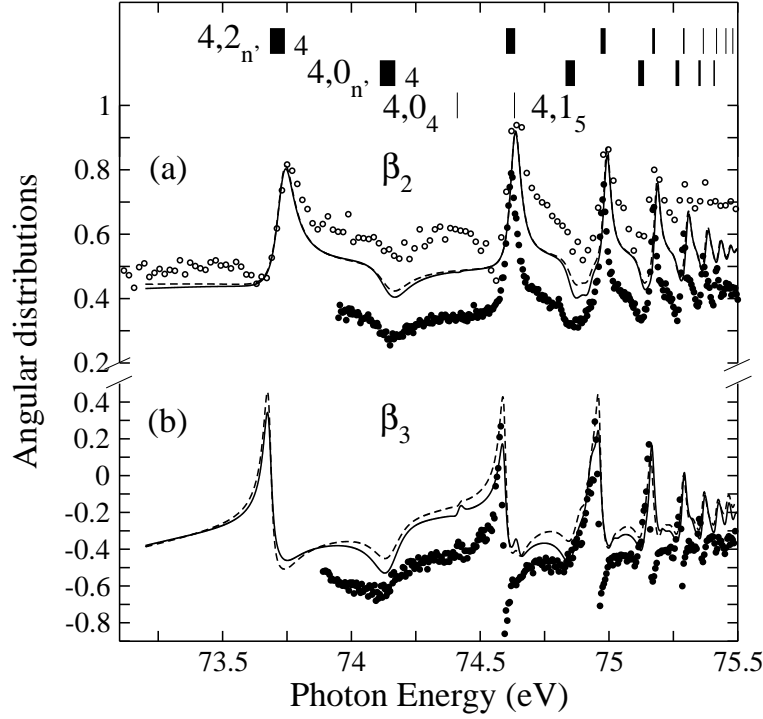


Figure 6.12: Angular distribution parameters (a)  $\beta_2$  and (b)  $\beta_3$  in the energy region from 73.1 to 75.5 eV, convoluted with a Gaussian of 12 meV. •, experimental data from Ref. [34]; ○, those from Ref. [122]. For further details, see Fig. 6.1.

Hayes and Scott [121] have also performed calculations of  $\beta_2$ ,  $\beta_3$ ,  $\beta_{3p}$ , and  $\beta_{3d}$ . However, considerable differences can be found between the two available calculations, e.g. some narrow peaks are missing in the calculated angular distribution parameters  $\beta_3$ ,  $\beta_{3p}$ , and  $\beta_{3d}$  of Hayes and Scott, such as the resonance 4,1<sub>5</sub>. The mimicking behavior of  $\beta_2$  and  $\beta_{2p}$  as well as of  $\beta_3$  and  $\beta_{3l}$  of the resonance of the principal series 4,2<sub>n'</sub> is shown in Fig. 6.11. It can also be understood on the basis of the mimicking behavior of the corresponding PCSs, as discussed before. With increasing energy, the overlap of 7 Rydberg series destroys the mimicking behavior. Although the present results are a considerable improvement compared to previously available theoretical calculations and experimental measurements, further advanced calculations and high-resolution measurements for  $l$ -specific ADPs are still necessary for this energy region.

In Fig. 6.12, the convoluted results for  $\beta_2$  and  $\beta_3$  are displayed together with experimental results of Menzel *et al.* [34] and Lindle *et al.* [103]. The present convoluted angular distribution parameters agree well with the theoretical results given in Ref. [34], which were obtained with the hyperspherical closed-coupling method. The  $\beta$ -values for both calculations are between the results of the two measurements presented in Fig. 6.12(a). The overall difference of 0.23 units between both experiments exceeds the given systematic experimental errors; as explained above, this could be due to non-dipolar effects. It should be mentioned that the energy positions of the resonances in  $\beta_2$  and  $\beta_3$  obtained in the present calculations show very good agreement with the experimental results of Lindle *et al.*

The present theoretical results have been published in Ref. [126]. Due to the absence of calculations for the  $n$ -specific ADPs below the SITs  $I_6$  and  $I_7$ , where our experiments had been performed (see previous chapter), the R-matrix method will be employed to calculate those ADPs in the near future.